Enhanced photonic spin Hall effect in a GST/HMM composite structure for optical encoding and refractive index sensing

Jie Cheng(程杰)[1*], Yangyang Gao(高扬阳)[1], Yiming Li(李一铭)[1], Fengfeng Chi(迟逢逢) [1], Haiyun Wang (王海云)[1] and Peng Dong(董鹏)[2*]

[1] *School of Science, Jiangsu Key Laboratory of Quantum Computing Science and Devices, Nanjing University of Posts and Telecommunications, Nanjing 210023, Jiangsu, China*

[2] *College of Electronic Information Engineering/College of Integrated Circuits, Research Center of Intelligent Sensor and Network Engineering Technology of Jiangsu Province, Nanjing University of Industry Technology, Nanjing, Jiangsu 210023, China*

**Corresponding author.*

E-mail address: *chengj@njupt.edu.cn* (Jie Cheng) and *2021101298@niit.edu.cn* (Peng Dong)

Conventional photonic devices are functionally frozen after fabrication, lacking dynamic reconfigurability. Hence, developing reconfigurable multi-functional devices on a single platform has become an urgent issue. The photonic spin Hall effect (PSHE), arising from spin-orbit interaction, offers a promising platform due to its sensitivity to external stimuli. In this work, we propose a PSHE-based multi-functional device with a GST/HMM composite structure, which enables dynamic switching between two-bit optical encoding and refractive index sensing by controlling the phase state of GST layer via external stimuli. In the amorphous GST state, the device enables two-bit encoding and wide-range refractive index sensing (1.0–1.5 RIU) with a sensitivity of 4.08×10^{-6} m/RIU. Switching GST to the crystalline state enhances the sensitivity to 5.32×10^{-5} m/RIU, more suitable for high-precision detection within a narrow-range of 1.00–1.10 RIU. These findings validate that the GST phase transition enables effective mode switching of the device, which paves the way for compact, multi-functional, and reconfigurable photonics.

Keywords：Photonic spin Hall effect, optical encoding, refractive index sensing, phase-change material, hyperbolic metamaterials.

PACS: 42.25.-p, 41.20.Jb, 42.79.-e, 78.20.Ci

1. Introduction

Driven by rapid progress in optical communications, integrated optics, and quantum information processing, modern optical systems are evolving toward higher integration density,

lower power consumption, and greater intelligence [1]. However, conventional photonic devices, once fabricated, are functionally frozen due to their fixed structures and material properties [2]. To overcome this limitation, photonic devices require a fundamental transformation from "single-function, static response" to "multi-functional integration, dynamic reconfigurability." Therefore, developing multi-functional photonic devices capable of dynamically switching between multiple functions on a single platform has become an urgent and imperative issue.

To realize such multi-functionality, one promising physical platform is the photonic spin Hall effect (PSHE) [3-5]. When linearly polarized light is reflected or refracted at an optical interface, the transverse splitting of spin components (left- and right-handed circularly polarized light) perpendicular to the incident plane occurs. This phenomenon, known as PSHE, results from the spin-orbit interaction between the photon spin (polarization) and the beam trajectory (orbital angular momentum) [6]. The PSHE has shown potential applications in precision metrology [7,8], image edge detection [9,10], optical encoding [11,12] and refractive index sensing [13,14]. More notably, due to the intrinsic sensitivity to external stimuli and the flexibility in spin-dependent manipulation, PSHE has recently inspired a new generation of multi-functional devices [15-19]. For instance, Cheng et al. developed a pressure-tunable PSHE sensor that can switch between different sensing tasks, such as cancer cell identification and oxyhemoglobin detection [15]. Meanwhile, two types of PSHE-based Janus sensors have been proposed for multi-tasking detection: one operating in the terahertz regime for thickness identification of graphene layer and waterborne bacterium sensing, and another operating in the short-wave infrared regime for wide-range pressure detection and cancer cell discrimination [16,18]. Additionally, by co-encoding resonant and geometric phases, spin-multiplexed dielectric metasurfaces with high PSHE efficiency of 92% and bifunctional wavefront control (anomalous refraction and focusing) were demonstrated [19].

Despite the progress in PSHE-based multi-functional devices, the integration of optical encoding and refractive index sensing into a single platform remains underexplored. Here, we address this challenge by combining a phase-change material (PCM) with a hyperbolic metamaterial (HMM) structure. Chalcogenide PCMs, particularly $Ge_2Sb_2Te_5$ (GST), are ideal for this application, owing to their pronounced and reversible optical contrast between the amorphous (aGST) and crystalline (cGST) phases [20,21]. Compared with other PCMs such as VO_2, GST offers several distinct advantages: it is non-volatile and maintains its state at room temperature for years

with zero static power [22,23], whereas VO_2 exhibits a volatile insulator–metal transition that reverts upon removal of the stimulus; it exhibits moderate optical loss in both phases, while VO_2 suffers from excessive absorption in its metallic state; and it supports more than 10^5 reversible phase-change cycles, providing superior long-term reliability compared with the limited cycling endurance of VO_2 [24]. These advantages collectively provide a compelling platform for achieving high-performance tunable and reconfigurable devices. In addition, hyperbolic metamaterials (HMM), composed of subwavelength-thick alternating planar metal and dielectric layers, exhibit extreme anisotropy with hyperbolic dispersions in the wavevector space [25], and have demonstrated a significant improvement in optical sensing [26,27]. Motivated by these advantages, we propose a PSHE-based device with a GST/HMM composite structure that actively switches between optical encoding and refractive index sensing by controlling the phase states of GST. The amorphous state enables two-bit encoding via the polarization state of incident light and the magnitude of PSHE displacements, while the crystalline state supports high-sensitivity refractive index sensing. This work paves the way toward compact, reconfigurable, and multi-functional photonic devices for future integrated optics.

2. Theory and model

To clarify the working principle of the proposed device, we first describe its geometric configuration and the physical mechanism of the PSHE. As schematically illustrated in Fig. 1, the device is based on a Kretschmann–Raether configuration consisting of a BK7 prism, a GST layer, a HMM composed of three alternating Au/ITO periods, and a bottom sensing region. Fig. 1(a) shows the layered structure of the GST/HMM composite, while Fig. 1(b) depicts the spin-dependent transverse splitting of the reflected beam, in which the left- and right-handed circularly polarized components separate along the y-axis. Fig. 1(c) illustrates the two distinct phases of GST, namely the aGST and cGST states, which can be reversibly switched by external stimuli.

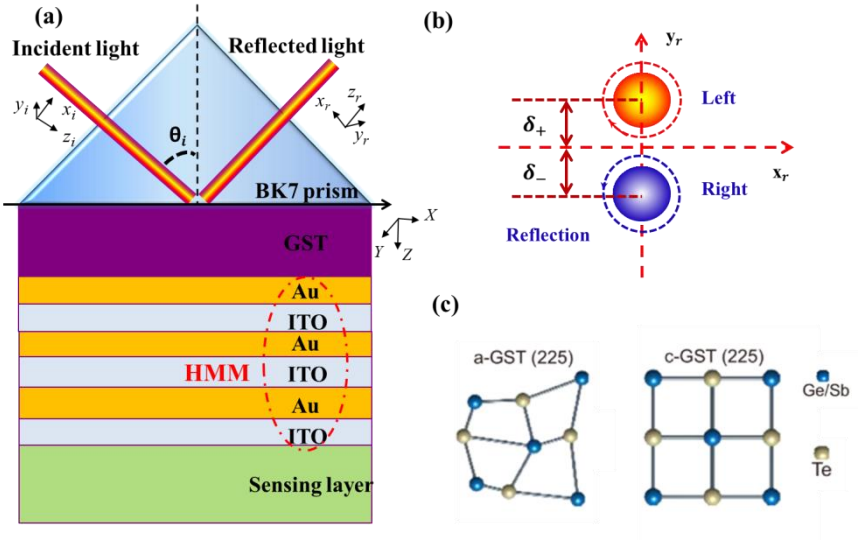


Fig.1 Schematic diagram for the proposed multi-functional device and corresponding PSHE. (a) The GST/HMM composite structure. (b) The description of spin-dependent transverse splitting for PSHE in reflected beams. (c) The representation of GST in its two distinct phases: aGST and cGST.

In this structure, the refractive index of BK7 prism is expressed by the Sellmeier equation [28]

$$n_{BK7}{}^2 = 1 + \frac{1.03961212\lambda^2}{\lambda^2 - 0.00600069867} + \frac{0.231792344\lambda^2}{\lambda^2 - 0.0200179144} + \frac{1.01046945\lambda^2}{\lambda^2 - 103.560653} \quad (1)$$

The GST layer can be deposited onto the base of BK7 prism through the physical vapor deposition technique, forming the second layer. The complex refractive index of GST ($n_{GST} = n + ik$) in both its amorphous and crystalline phases can be obtained via spectroscopic ellipsometry technique [20], as displayed in Fig. 2. Obviously, both the real and imaginary parts of the refractive index exhibit significant dispersion over the entire visible-near infrared spectral ranges. The substantial refractive index contrast between aGST and cGST is attributed to the chemical bonding transformation from covalent (amorphous) to resonant (crystalline) [29]. The ability of GST to reversibly trigger this structural phase transition via thermal, electrical, or optical stimuli [20], renders it an exceptional platform for achieving dynamic tunability and functional integration.

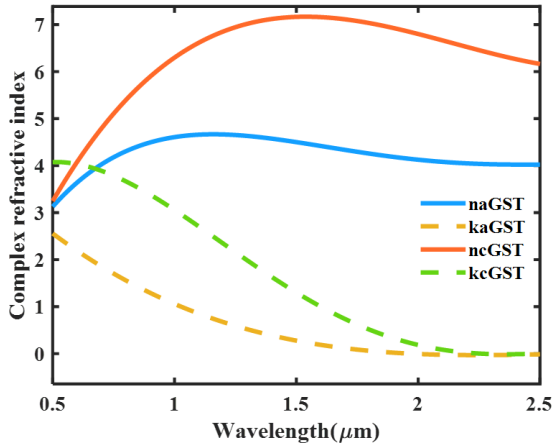


Fig. 2 The complex refractive index of GST for both the amorphous and crystalline phases.

In our model, three periods of metal (Au)/dielectric (ITO) bilayer constitute the HMM, and the bilayer thickness is only 20 nm, far smaller than the operating wavelength. In practical experiments, the thickness of each layer can be precisely controlled by adjusting the sputtering power and deposition time during magnetron sputtering. The long-wave limit permits the extraction of both parallel and vertical components of the HMM permittivity via the effective medium theory (EMT) [27]

$$\varepsilon_x = p\varepsilon_{Au} + (1-p)\varepsilon_{ITO} \tag{2}$$

$$\varepsilon_z^{-1} = p\varepsilon_{Au}^{-1} + (1-p)\varepsilon_{ITO}^{-1} \tag{3}$$

$$p = \frac{d_{Au}}{d_{Au}+d_{ITO}} \tag{4}$$

where ε_x and ε_z denote the parallel and vertical components of the HMM permittivity, respectively; ε_{Au} and ε_{ITO} represent the permittivity of Au and ITO, which are obtained from Ref [30] and [31], respectively; d_{Au} and d_{ITO} represent their corresponding thickness, respectively; p denotes the metal filling fraction, which is defined as the ratio of the metal layer thickness to a pair of metal/dielectric HMM thickness. From Fig. 3(a) and (b), the real part of HMM permittivity along x and z axes show opposite signs: $\varepsilon_{rx} < 0$ and $\varepsilon_{rz} > 0$ when $600\ \text{nm} \leq \lambda \leq 1600\ \text{nm}$, indicating the HMM holds a hyperbolic dispersion with p varying from 0.3 to 0.7. Fig. 3(c) illustrates the dispersion curves of k_x and k_z at a wavelength of 1550 nm, which exhibit hyperbolic behavior as described by $k_x^2/\varepsilon_z + k_z^2/\varepsilon_x = k_0^2$.

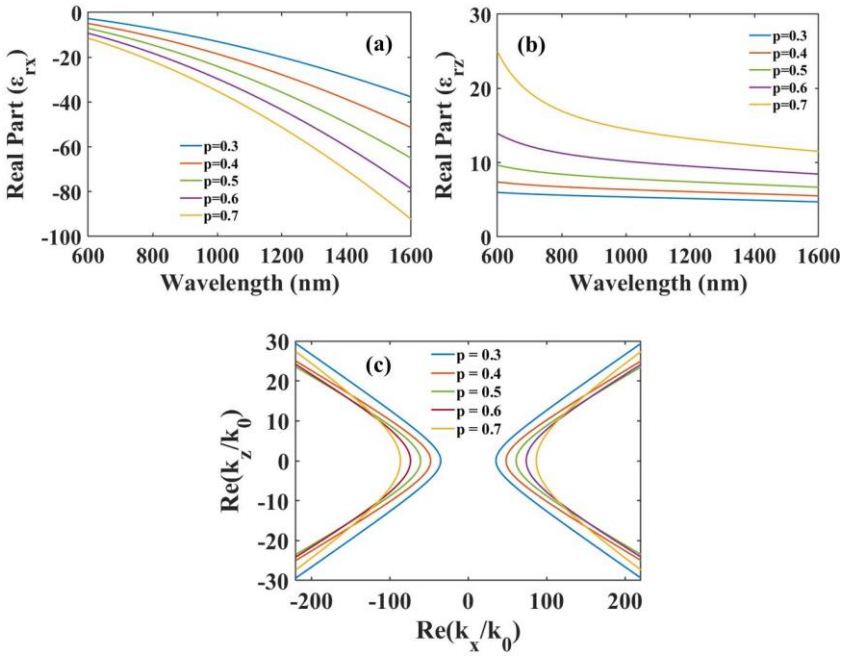


Fig. 3 (a) and (b) Wavelength dependence of the real parts of ε_x and ε_z for Au/ITO HMM when p varies from 0.3 to 0.7. (c) The real part relation curves between k_x/k_0 and k_z/k_0 with the wavelength of 1550 nm.

The monochromatic Gaussian beam is incident on the GST/HMM structure with an incident angle of θ_i, as shown in Fig. 1(a), and the PSHE of reflected light appears leading to the splitting of left- and right-handed circularly polarized components in the y axis direction (in Fig. 1(b)). Based on the angular spectrum theory, we describe the incident Gaussian beam as [32]

$$\widetilde{\boldsymbol{E}}_i(k_{ix}, k_{iy}) = \frac{w_0}{\sqrt{2\pi}} \exp\left[-\frac{(k_{ix}^2+k_{iy}^2)w_0^2}{4}\right] \tag{5}$$

where w_0 is the beam waist. k_{ix} and k_{iy} are the wave-vector components of the incident light in the x and y directions, respectively. The relationship between the reflected and incident angular spectra can be derived as [32]

$$\begin{bmatrix}\widetilde{\boldsymbol{E}}_r^H \\ \widetilde{\boldsymbol{E}}_r^V\end{bmatrix} = \begin{bmatrix} r_p & \frac{k_{ry}\cot\theta_i(r_p+r_s)}{k_0} \\ -\frac{k_{ry}\cot\theta_i(r_p+r_s)}{k_0} & r_s \end{bmatrix} \begin{bmatrix}\widetilde{\boldsymbol{E}}_i^H \\ \widetilde{\boldsymbol{E}}_i^V\end{bmatrix} \tag{6}$$

Here, $\widetilde{\boldsymbol{E}}_r^{H,V}$ and $\widetilde{\boldsymbol{E}}_i^{H,V}$ denote the horizontal (H) and vertical (V) components of the angular spectra for the reflected and incident light beams, respectively. k_0 is the wave number in free space. The coefficients $r_{p,s}=|r_{p,s}|exp(i\phi_{p,s})$ are the Fresnel reflection coefficients for p- and s-polarized waves, respectively, which can be calculated by the transfer matrix method [32].

The transverse shift of reflected light are given by [33]

$$\delta_{\pm}^{H,V} = \frac{\iint y_r \left|\boldsymbol{E}_{r\pm}^{H,V}\right|^2 dx_r dy_r}{\iint \left|\boldsymbol{E}_{r\pm}^{H,V}\right|^2 dx_r dy_r} \tag{7}$$

From Equations (5) to (7), the spin-dependent shift of the reflected light due to the photonic SHE can be expressed as [33]

$$\delta_{\pm}^{H} = \mp \frac{k_0 w_0^2 \mathrm{Re}\left(1+\frac{r_s}{r_p}\right)\cot\theta_i}{k_0^2 w_0^2 + \left|\frac{\partial \ln r_p}{\partial \theta_i}\right|^2 + \left|\left(1+\frac{r_s}{r_p}\right)\cot\theta_i\right|^2} \tag{8}$$

$$\delta_{\pm}^{V} = \mp \frac{k_0 w_0^2 \mathrm{Re}\left(1+\frac{r_p}{r_s}\right)\cot\theta_i}{k_0^2 w_0^2 + \left|\frac{\partial \ln r_s}{\partial \theta_i}\right|^2 + \left|\left(1+\frac{r_p}{r_s}\right)\cot\theta_i\right|^2} \tag{9}$$

where ± denotes the left- and right-handed circular polarization components, respectively.

3. Results and discussion

For the GST/HMM system, the PSHE can be effectively modulated by actively switching the phase states of GST. Leveraging this tunable PSHE response, the device holds promise for realizing multi-functional applications on a single integrated platform. In the following calculation, the parameters are chosen as follows: the incident wavelength is 1550 nm; the beam waist is 30 λ; and the metal filling fraction p of HMM is 0.4.

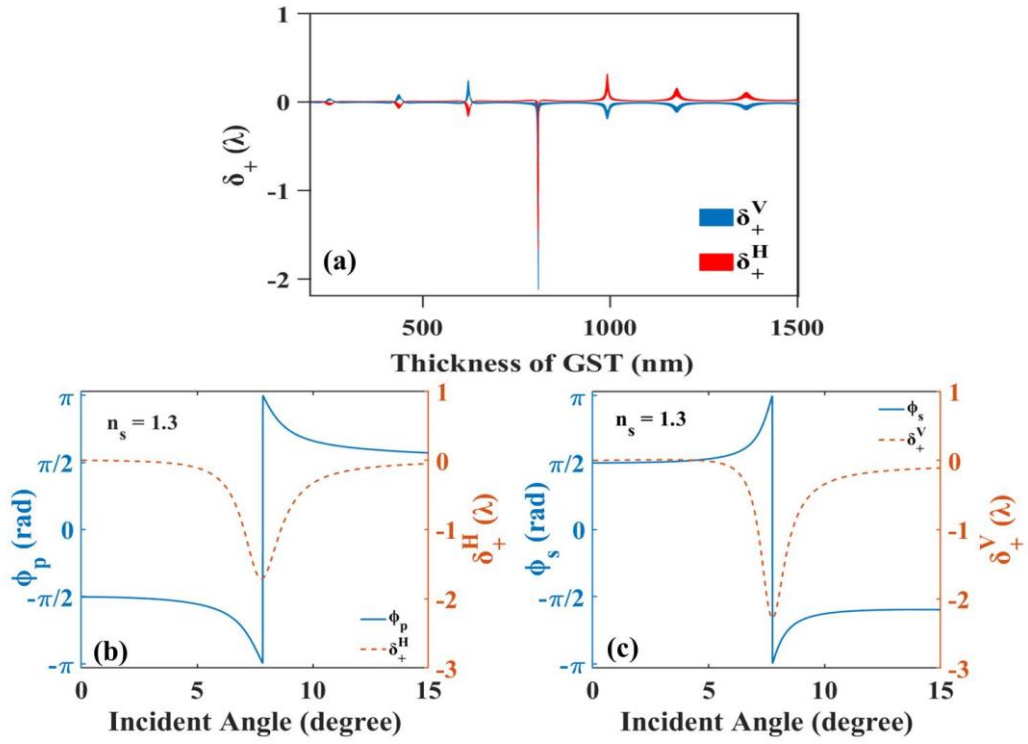


Fig. 4 (a) The transverse shift of PSHE $\delta_{+}^{H,V}$ as a function of GST thickness d_{GST}. The GST is in its amorphous phase, and the refractive index of sensing layer n_s sets as 1.3. (b) and (c) The reflection phase $\phi_{p,s}$ and transverse shift $\delta_{+}^{H,V}$ versus the incident angle.

When GST is in the amorphous state, the proposed device can be employed for two-bit encoding and wide-range refractive index sensing. To ensure considerable shifts for both H and V polarizations, the relationship between the transverse shifts $\delta_+^{H,V}$ and the GST layer thickness d_{GST} is shown in Fig. 4(a), at a sensing refractive index n_s of 1.3. Over most of the thickness range (200–1500 nm), both δ_+^H and δ_+^V remain near zero, with pronounced peaks or valleys only at specific values, demonstrate that PSHE is highly sensitive to the thickness of GST layer. The most significant response for both polarizations occurs near $d_{GST} = 802\ nm$, therefore, we adopt this GST thickness for further investigation. To understand the origin of this pronounced PSHE valley, we present Fig. 4(b) and (c), which plot the reflection phase $\phi_{p,s}$ and transverse shift $\delta_+^{H,V}$ versus the incident angle. A distinct phase jump of $\phi_{p,s}$ near 8° is observed for both *H* and *V* polarizations. This enhanced phase jump results from the interlayer coupling modes of surface plasmon polaritons in our Au/ITO multilayer HMM, which is distinct from the single-metal-layer design of the conventional Kretschmann–Raether configuration, ultimately giving rise to a prominent PSHE valley.

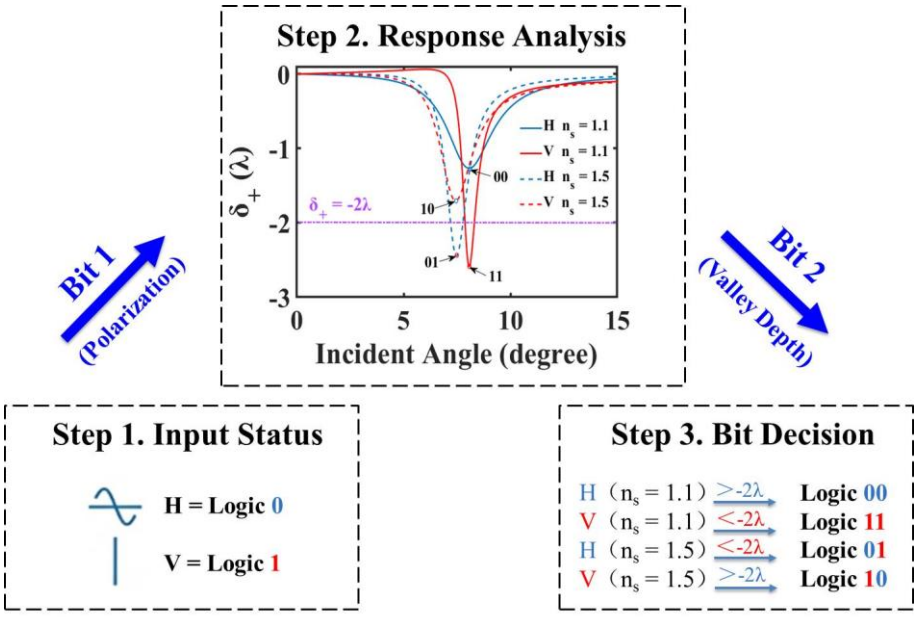


Fig. 5 Schematic illustration of the two-bit encoding.

Developing new optical coding technology is important and highly desired due to its potential applications in information protection and communication [34]. In particular, multi-bit optical encoding, which exploits physical dimensions such as polarization, wavelength, and angle, is indispensable for optical communications, optical logic gates, and reconfigurable photonic devices [11,35]. Here, with the GST layer in its amorphous state, we investigate the behavior of PSHE shift

by jointly tuning the refractive index of sensing layer and the input polarization state, thereby realizing a two-bit optical encoding scheme. The schematic diagram illustrating the principle of the two-bit encoding is presented in Fig. 5. First, we define the polarization states of incident light, where H-polarized light is assigned as logic 0 and V polarization as logic 1. Then the behavior of the transverse shift $\delta_+^{H,V}$ as a function of the incident angle is examined for both H and V polarizations. The PSHE curves for the four combined states, namely (H, n_s = 1.1), (V, n_s = 1.1), (H, n_s= 1.5), and (V, n_s = 1.5), all exhibit a valley-type response, but with different valley depths of -1.2 λ, -2.7 λ, -2.3 λ, and -1.7 λ, respectively. This indicates that the PSHE shift can be modulated by both the input polarization state and the refractive index of sensing layer. Subsequently, a decision line at δ_+ = -2 λ is introduced to discretize the four states. For n_s = 1.1, the PSHE valley of H-polarized light resides above -2 λ, while that of V-polarized light falls below -2 λ. For n_s = 1.5, the opposite occurs: the H-polarized valley is below -2 λ and the V-polarized valley above -2 λ. Following this scheme, the four combined states can be respectively mapped to four distinct binary outputs:H ($n_s = 1.1$) → Logic 00, V ($n_s = 1.1$) → Logic 11, H ($n_s = 1.5$) → Logic 01, V ($n_s = 1.5$) → Logic 10. In contrast to conventional encoding schemes that depend on a single optical intensity or a single input state, this approach not only doubles the information capacity but also exhibits superior performance in anti-interference and information fusion.

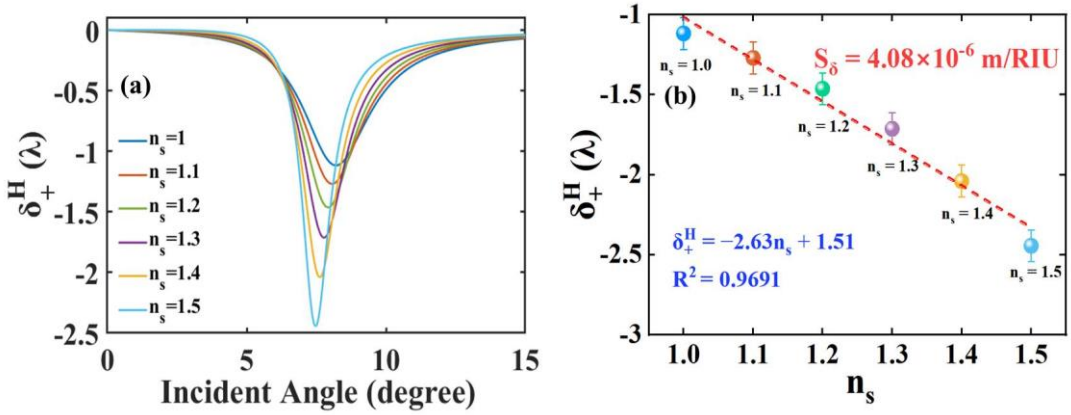


Fig. 6 The sensing performance for aGST and n_s=1.0-1.5 RIU. (a) Relationship between the δ_+^H and the incident angle at different n_s values. (b) Linear fitting of the PSHE valley and n_s.

In addition to the two-bit encoding, the proposed device also shows potential for wide-range refractive index sensing when the GST layer is its amorphous state. Here, taking H-polarized light as an example, we present the significant response of PSHE shift over a wide refractive index

range of 1.0-1.5 RIU. As shown in Fig. 6(a), the δ_+^H curves all exhibit a distinct valley near a specific incident angle, and the δ_+^H is highly sensitive to the refractive index change of sensing layer. When n_s increases from 1.0 to 1.5, the valley depth increases monotonically from -1.15 λ to -2.46 λ. Consequently, by extracting the valley depth of δ_+^H, the refractive index of sensing layer can be directly retrieved, thereby enabling wide-range refractive index sensing. To quantitatively evaluate the sensing performance of this PSHE-based sensor, the sensitivity can be defined as $S_\delta = \frac{\Delta\delta}{\Delta n_s}$, where Δn_s is the refractive index variation of sensing layer, and $\Delta\delta$ is the corresponding change in the extremum (peak or valley) of PSHE shift. The δ_+^H valley versus n_s is plotted in Fig. 6(b), which exhibits a nearly linear relationship. To provide a clearer description of sensing performance, a linear fitting is applied, yielding a sensitivity of 4.08×10^{-6} m/RIU. Furthermore, the coefficient of determination R^2 is 0.9691, demonstrating the high reliability of the proposed GST/HMM sensor for wide-range refractive index detection.

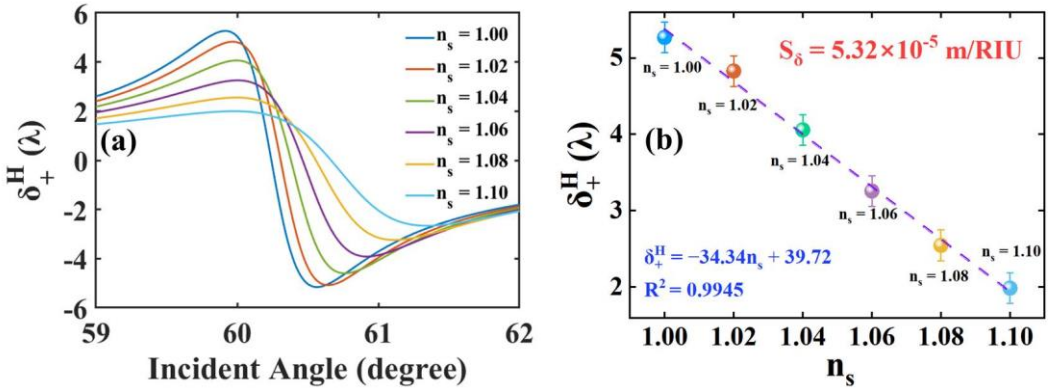


Fig. 7 The sensing performance for cGST and n_s=1.00-1.10 RIU. (a) Relationship between the δ_+^H and the incident angle at different n_s values. (b) Linear fitting of the PSHE peak and n_s.

Although the GST/HMM device is capable of refractive index detection in the GST amorphous state, the sensitivity remains modest. To overcome this, we actively trigger a phase transition, switching the GST layer to its crystalline state. As depicted in Fig. 7, under the crystalline GST condition, the PSHE shift for H-polarized light varies significantly with the refractive index of sensing layer. As n_s increases from 1.00 to 1.10, both the peak and valley of δ_+^H curves gradually decrease. This implies that the δ_+^H is capable of providing a continuous and distinguishable response to changes in the refractive index. Fig. 7(b) shows a good linear relationship between δ_+^H peak and the refractive index n_s, with the fitting expression given by δ_+^H= -34.34n_s + 39.72 and a coefficient of determination R^2 = 0.9945. The corresponding

sensitivity is determined to be 5.32×10^{-5} m/RIU. Evidently, the crystalline GST configuration of our proposed device yields a substantially higher sensitivity than the amorphous case (approximately 13 times), accompanied by an improved linear fitting quality. These results demonstrate that, in the crystalline GST phase, the PSHE device realizes both sensitive and reliable refractive index sensing.

It is worth noting that the amorphous and crystalline GST configurations of this GST/HMM device are suited for different sensing tasks: the amorphous state enables wide-range detection (1.0–1.5 RIU) with moderate sensitivity, whereas the crystalline state offers high-precision detection within a narrow range (1.00–1.10 RIU). It is worth noting that the HMM in this work consists of three periods of Au/ITO, with the metal filling ratio fixed at 0.4. Subsequent adjustment of the above parameters and replacement of the BK7 prism with other high-refractive-index prisms are expected to modify and further enhance the sensitivity. This complementarity in refractive index sensing, together with the two-bit encoding capability in the amorphous state, demonstrates that the phase transition of GST not only manipulates the operating mode of the device but also offers tunable performance advantages for diverse application scenarios.

4. Conclusion

The PSHE-based multi-functional device with a GST/HMM composite structure is proposed, which enables the integration of two-bit optical encoding and high-sensitivity refractive index sensing via GST phase transition. In the amorphous state, by jointly tuning the input polarization state and the refractive index of the sensing layer, the device achieves two-bit encoding by setting a decision line for PSHE shifts. Meanwhile, it offers wide-range refractive index detection (1.0–1.5 RIU) with a sensitivity of 4.08×10^{-6} m/RIU. In the crystalline state, the sensitivity for the refractive index range of 1.00–1.10 RIU is substantially enhanced to 5.32×10^{-5} m/RIU (approximately 13 times that of the amorphous condition), making it more suitable for high-precision detection within a narrow range. These results confirm that the phase transition of GST effectively manipulates the operating mode of the device and offers tunable performance advantages for diverse applications, providing a promising route toward compact, multi-functional, and reconfigurable photonic devices.

Funding

This work was partially supported by the National Natural Science Foundation of China (Grant No. NSFC 12175107); the Qing Lan Project of Jiangsu Province, China; and the open research grant program by Research Center of Intelligent Sensor and Network Engineering Technology of Jiangsu Province (ZK25-15-03).

Declaration of Competing Interest

The authors declare that they have no known competing financial interests or personal relationships that could have appeared to influence the work reported in this paper.

Data availability

Data will be made available on request.

References

[1] Dutta T, Safinezhad A, Zhudybina M, Garro I L, Velázquez-González J S, Sharma A K, Ung B and Mishra S K 2025 *J. Mater. Chem. C* **13** 11521-11561

[2] Kim J, Kim J Y, Kim J, Hyeong Y, Neseli B, You J B, Shim J, Shin J, Park H H and Kurt H 2025 *Nanophotonics* **14** 121-151

[3] Hosten O and Kwiat P 2008 *Science* **319** 787-790

[4] Sheng L J, Chen Y, Yuan S J, Liu X Q, Zhang Z Y, Jing H, Kuang L M and Zhou X X 2023 *Prog. Quantum Electron.* **91-92** 100484

[5] Ling X H, Zhou X X, Huang K, Liu Y C, Qiu C W, Luo H L and Wen S C 2017 *Rep. Prog. Phys.* **80** 066401

[6] Bliokh K Y, Rodríguez-Fortuño F J, Nori F and Zayats A V 2015 *Nat. Photon.* **9** 796-808

[7] Zhou X X, Ling X H, Luo H L and Wen S C 2012 *Appl. Phys. Lett.* **101** 251602

[8] Chen S Z, Zhou X X, Ling X H, Shu W X, Luo H L and Wen S C 2021 *Appl. Phys. Lett.* **118** 111104

[9] Zhu T F, Lou Y J, Zhou Y H, Zhang J H, Huang J Y, Li Y, Luo H L, Wen S C, Zhu S Y, Gong Q H, Qiu M and Ruan Z C 2019 *Phys. Rev. Appl.* **11** 034043

[10] Zhang J, Zhou S, Dai X, Huang M and Yu X Y 2023 *Opt. Express* **31** 6062-6075

[11] Pei N, Zheng Y, Tang Y Q, Tang X Z and Zhang H F 2025 *Mater. Des.* **255** 114218

[12] Hong J H, Chen Z H, Lin S, Chen Y and Zhou X X 2023 *Ann. Phys. (Berlin)* **535** 2200515

[13] Cheng J, Li Y M, Wang Z J, Gao Y Y and Liu S L 2026 *J. Mater. Chem. C* **14** 5505

[14] Ahlawat L, Kishor K and Sinha R K 2024 *Opt. Laser Technol.* **170** 110183

[15] Cheng J, Cheng C, Li Z K and Liu S L 2025 *Sens. Actuators A: Phys.* **390** 116625

[16] Sui J Y, Zou J H, Liao S Y, Li B X and Zhang H F 2023 *Appl. Phys. Lett.* **122** 231105

[17] Cheng J, Li R Z, Cheng C, Zhang Y L, Liu S L and Dong P 2024 *Chin. Phys. B* **33** 074203

[18] Sui J Y, Zou J H, Liao S Y, Wan B F and Zhang H F 2024 *IEEE Trans. Instrum. Meas.* **73** 7000109

[19] Wang Z, Yao Y, Pan W K, Zhou H Y, Chen Y Z, Lin J, Hao J M, Xiao S Y, He Q, Sun S L and Zhou L 2023 *Adv. Sci.* **10** 2205499

[20] Aly A H, Awasthi S K, Mohamed A M, Al-Dossari M, Matar Z S, Mohaseb M A, El-Gawaad N S A and Amin A F 2021 *Phys. Scr.* **96** 125533
[21] Fang Y, Furniss D, Jayasuriya D, Parnell H, Tang Z Q, Gibson D, Bayya S, Sanghera J, Seddon A B and Benson T M 2019 *Opt. Mater.: X* **2** 100030
[22] Li P N, Yang X S, Maβ T W W, Hanss J, Lewin M, Michel A K U, Wuttig M and Taubner T 2016 *Nat. Mater.* **15** 870-875
[23] Zhang Y F, Chou J B, Li J Y, Li H S, Du Q Y, Yadav A, Zhou S, Shalaginov M Y, Fang Z R, Zhong H K, Roberts C, Robinson P, Bohlin B, Ríos C, Lin H T, Kang M, Gu T, Warner J, Liberman V, Richardson K and Hu J J 2019 *Nat. Commun.* **10** 4279
[24] Bruns G, Merkelbach P, Schlockermann C, Salinga M, Wuttig M, Happ T D, Philipp J B and Kund M 2009 *Appl. Phys. Lett.* **95** 043108
[25] Takayama O, Sukham J, Malureanu R, Lavrinenko A V and Puentes G 2018 *Opt. Lett.* **43** 4602-4605
[26] Sreekanth K V, Alapan Y, Elkabbash M, Llker E, Hinczewski M, Gurkan U A, Luca A D and Strangi G 2016 *Nat. Mater.* **15** 621-627
[27] Hu S Q, Shi W C, Chen Y, Chen Y F, Liu G S, Chen L, Luo Y H and Chen Z 2022 *J. Lightwave Technol.* **40** 887-893
[28] Weber M J 2018 *Handbook of Optical Materials* Boca Raton: CRC Press
[29] Xu M, Cheng Y Q, Sheng H W and Ma E 2009 *Phys. Rev. Lett.* **103** 195502
[30] Johnson P B and Christy R W 1972 *Phys. Rev. B* **6** 4370-4379
[31] Chen Q, Song S, Wang H, Liang L, Dong Y and Wen L 2021 *Nano Res.* **14** 2673-2680
[32] Luo H L, Ling X H, Zhou X X, Shu W X, Wen S C and Fan D Y 2011 *Phys. Rev. A* **84** 033801
[33] Tan X J and Zhu X S 2016 *Opt. Lett.* **41** 2478-2481
[34] Ouyang C, Zhang Y Q, Yang D P, Ma D K and Huang S M 2021 *J. Mater. Chem. C* **9** 4466-4473
[35] Xu H R, Zhang T H, Wan B F and Zhang H F 2024 *AIP Adv.* **14** 105301